Supplementary Information

3D-Printed Epidermal Sweat Microfluidic Systems with Integrated Microcuvettes for Precise Spectroscopic and Fluorometric Biochemical Assays

Da Som Yang[1,2†], Yixin Wu[1,3†], Evangelos E. Kanatzidis[1,4†], Raudel Avila[5,6], Mingyu Zhou[1,7], Yun Bai[1,3], Shulin Chen[1,7], Yurina Sekine[8], Joohee Kim[1,9], Yujun Deng[5,10], Hexia Guo[1,3], Yi Zhang[11,12], Roozbeh Ghaffari[1,7,13], Yonggang Huang[1,3,5,14], and John A. Rogers[1,3,5,7,13,15-17*]

[1] Querrey Simpson Institute for Bioelectronics, Northwestern University, Evanston, IL 60208, United States
[2] Precision Biology Research Center (PBRC), Sungkyunkwan University, Suwon, 16419, South Korea
[3] Department of Materials Science and Engineering, Northwestern University, Evanston, IL 60208, United States
[4] Department of Molecular Biosciences, Northwestern University, Evanston, IL, USA
[5] Department of Mechanical Engineering, Northwestern University, Evanston, IL 60208, United States
[6] Department of Mechanical Engineering, Rice University, Houston, TX, 77005, United States
[7] Department of Biomedical Engineering, Northwestern University, Evanston, IL 60208, United States
[8] Materials Sciences Research Center, Japan Atomic Energy Agency, Tokai, Ibaraki 319-1195, Japan
[9] Center for Bionics of Biomedical Research Institute, Korea Institute of Science and Technology, Seoul, 02792 Republic of Korea
[10] State Key Laboratory of Mechanical System and Vibration, Shanghai Jiao Tong University, Shanghai, China
[11] Polymer Program, Institute of Materials Science, University of Connecticut, Storrs, Connecticut 06269, United States
[12] Department of Biomedical Engineering, University of Connecticut, Storrs, Connecticut 06269, United States
[13] Epicore Biosystems Inc., Cambridge, MA, USA
[14] Department of Civil and Environmental Engineering, Northwestern University, Evanston, IL 60208, USA
[15] Department of Neurological Surgery, Northwestern University, Evanston, IL 60208, United States
[16] Department of Electrical and Computer Engineering, Northwestern University, Evanston, IL 60208, United States
[17] Department of Chemistry, Northwestern University, Evanston, IL 60208, United States

*Corresponding author. Email: jrogers@northwestern.edu (J.A.R.)
†These authors contributed equally to this work.

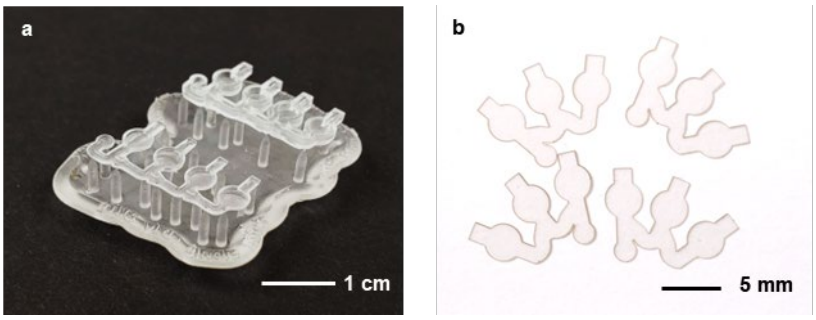

Supplementary figure 1. a. Photograph of 3D-printed microcuvettes with supporting frameworks. b. Photograph of adhesive layers after patterning with a CO_2 laser.

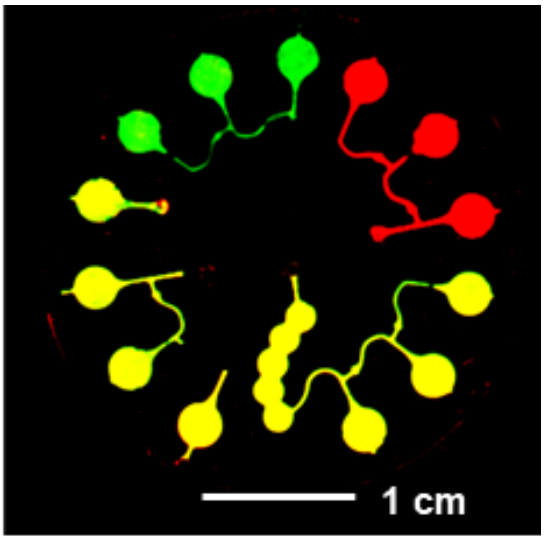

Supplementary figure 2. Fluorescence image of a 3D-printed sweat microfluidic system with integrated microcuvettes filled with fluorescent dyes.

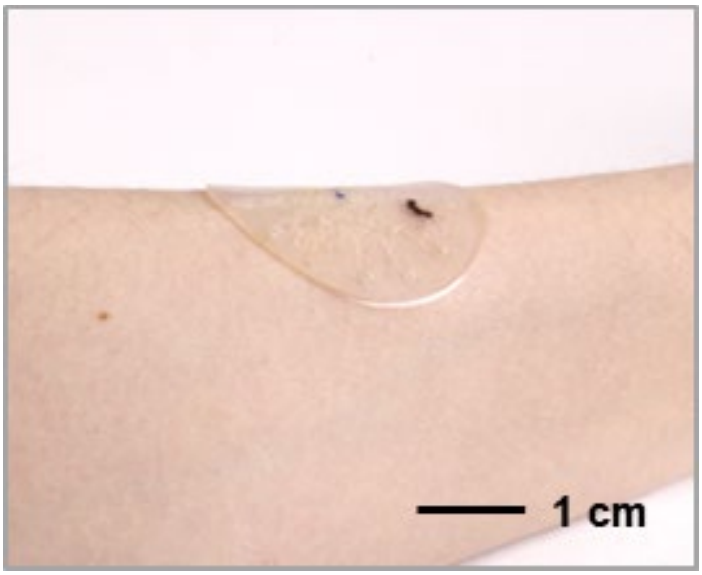

Supplementary figure 3. Photograph of a thin 3D-printed sweat microcuvettes encapsulated system mounted on the skin of the arm.

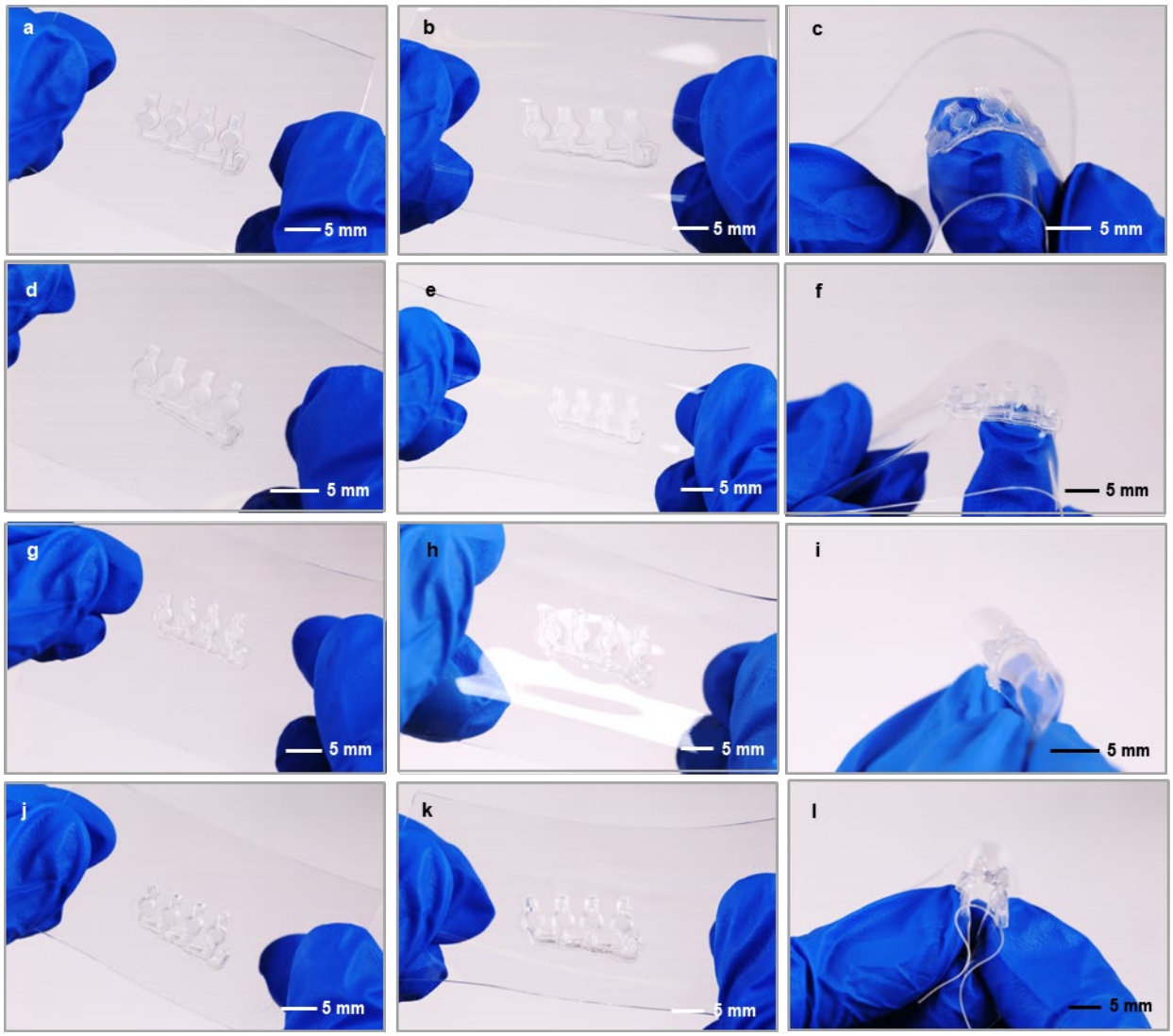

Supplementary figure 4. Photographs of encapsulated microcuvettes systems made of two types of polymer resins (MA-MA and Acrylate-IBA) with two thicknesses (200 µm and 1 mm). a-c. Photographs of thin microcuvettes (200 µm) made of MA-MA without deformation (a), stretched (b), and bent (c). d-f) Photographs of thick microcuvettes(1 mm) made of MA-MA without deformation (d), stretched (e), and bent (f). (g-i) Photographs of thin microcuvettes (200 µm) made of Acrylate-IBA without deformation (g), stretched (h), and bent (i). (j-l) Photographs of thick microcuvettes (1 mm) made of Acrylate-IBA without deformation (j), stretched (k), and bent (l).

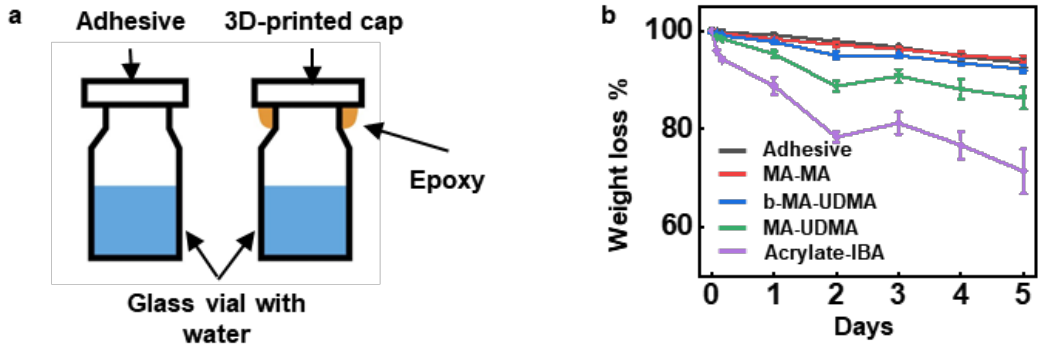

Supplementary figure 5. a. Schematic illustration of a comparison experiment that involves glass vials with water sealed by either an adhesive or 3D-printed cap structure with the same thickness as the microcuvettes (200 μm). **b**. Weight loss due to evaporation of the water as a function of time in days for the case of cap structures made with different polymer resins.

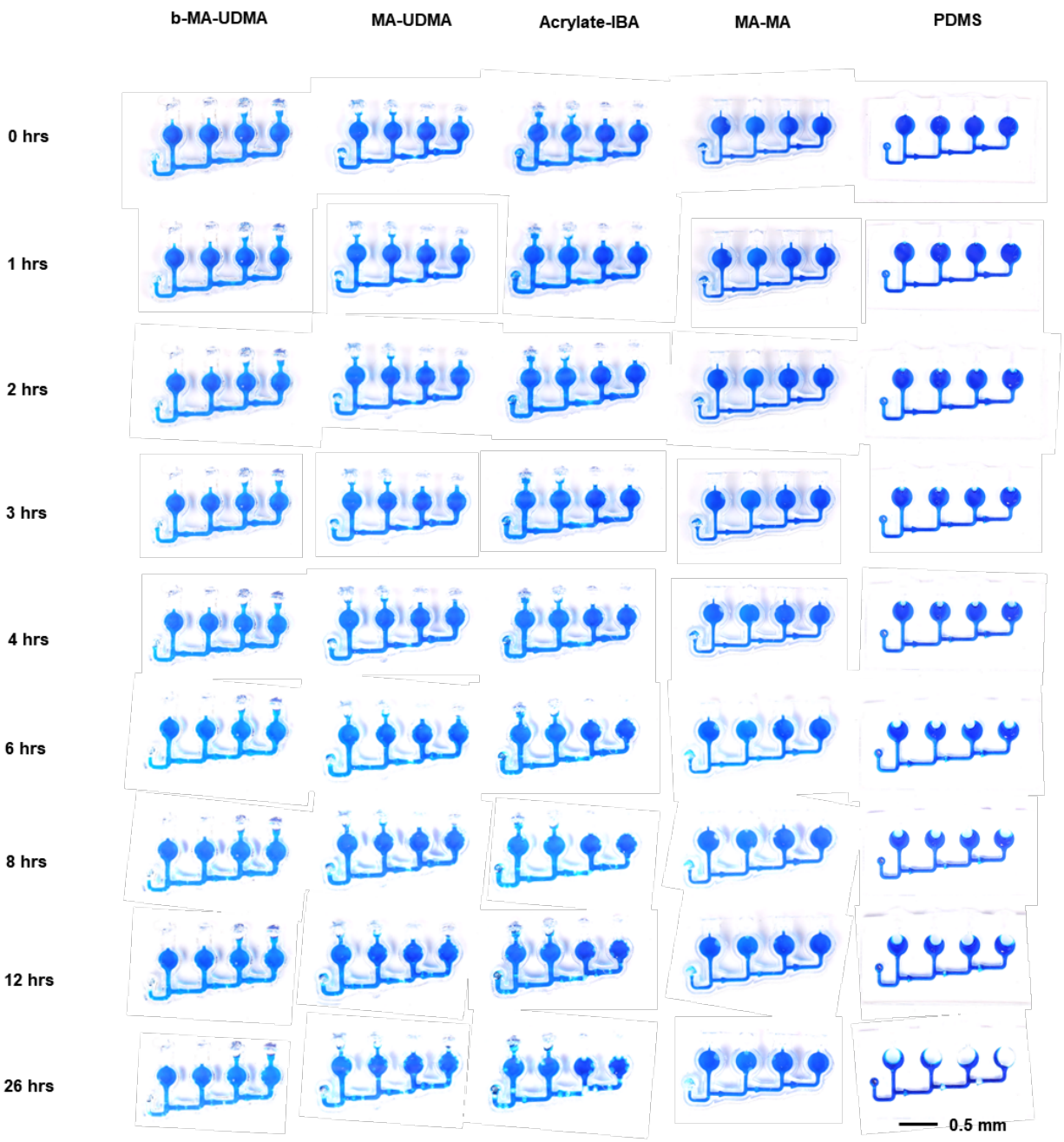

Supplementary figure 6. Sequence of images of microcuvettes fill with aqueous solutions of blue dye as a function of time. The bubbles appear due to water evaporation for cases of four different polymer resins.

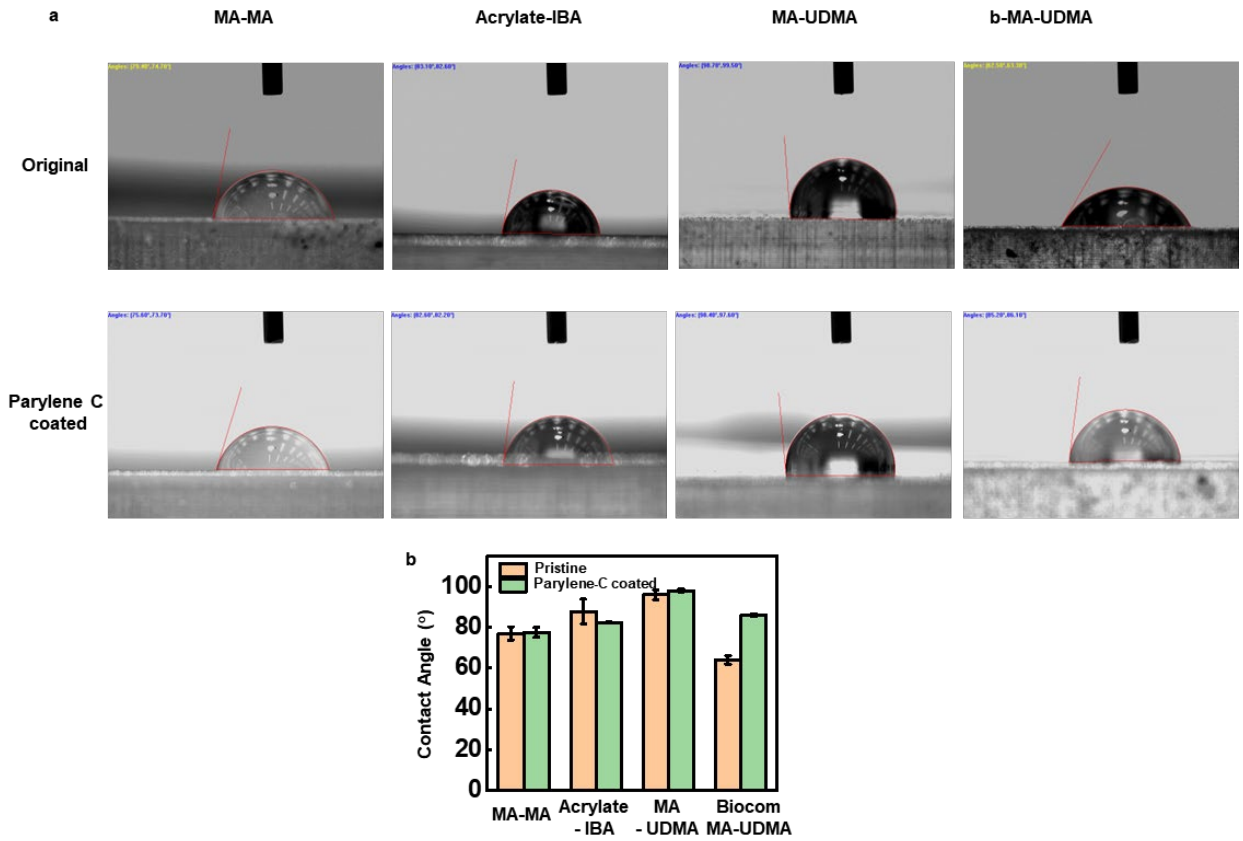

Supplementary figure 7. Contact angle of 3D-printed microcuvettes formed using different resins. a,b. Photographs (a) and bar graph (b) of contact angle on pristine and Parylene-C coated microcuvettes printed in different polymer resins (MA-MA, Acrylate- IBA, MA-UDMA, b-MA-UDMA).

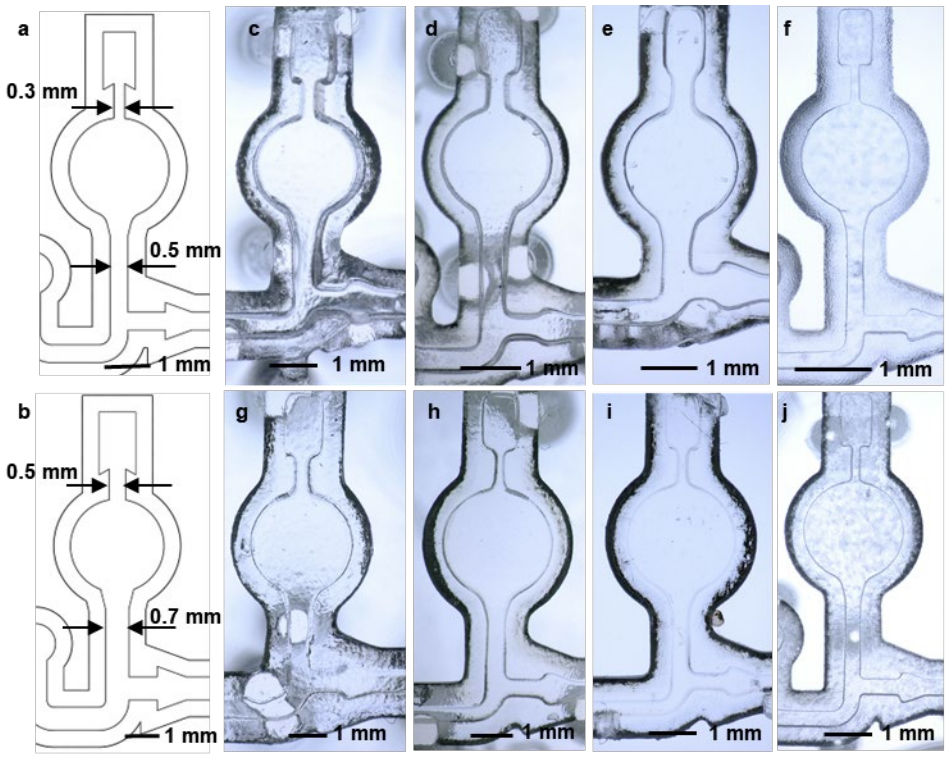

Supplementary figure 8. Optical micrographs of 3D-printed microcuvettes formed with four different resins. a,b. CAD drawings of the skeleton. c-f. Optical micrographs of thick skeletons (1 mm) printed with Acrylate-IBA (c), MA-UDMA (d), b-MA-UDMA (e) and MA-MA (f). g-j. Optical micrographs of thin skeletons (200 µm) printed with Acrylate-IBA (g), MA-UDMA (h), b-MA-UDMA (i) and MA-MA (j).

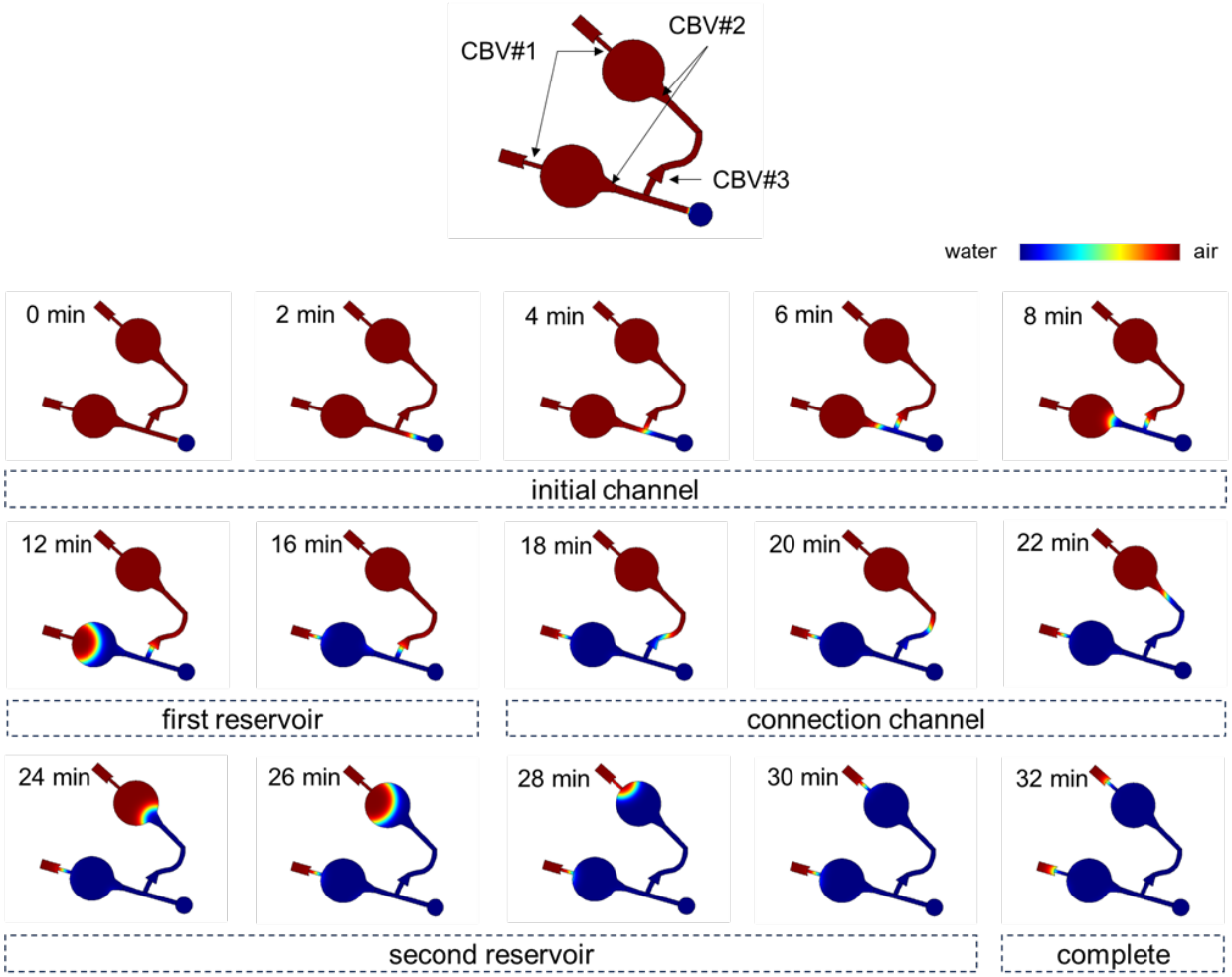

Supplementary figure 9. The simulated moving air/swear interface over 30 minutes showing the sequential filling process controlled by the CBVs.

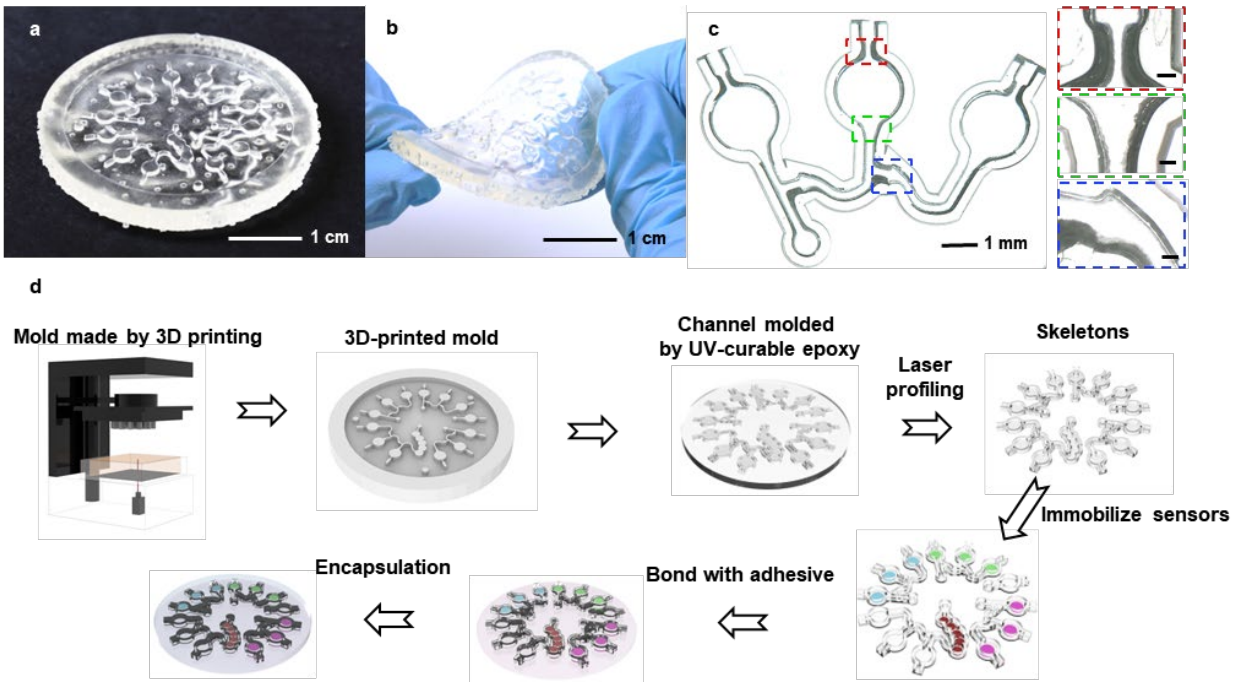

Supplementary figure 10. 3D-printed mold for fabrication of sweat microcuvettes systems. a. Photograph of a 3D-printed elastic mold made of Acrylate-IBA. b. Photograph of a twisted 3D-printed Acrylate-IBA mold. c. Optical micrographs of a NOA microcuvettes made from a 3D-printed elastic mold. Scale bar for the right figures: 100 μm. d. Fabrication process for a sweat microcuvettes system made from a 3D-printed Acrylate-IBA mold.

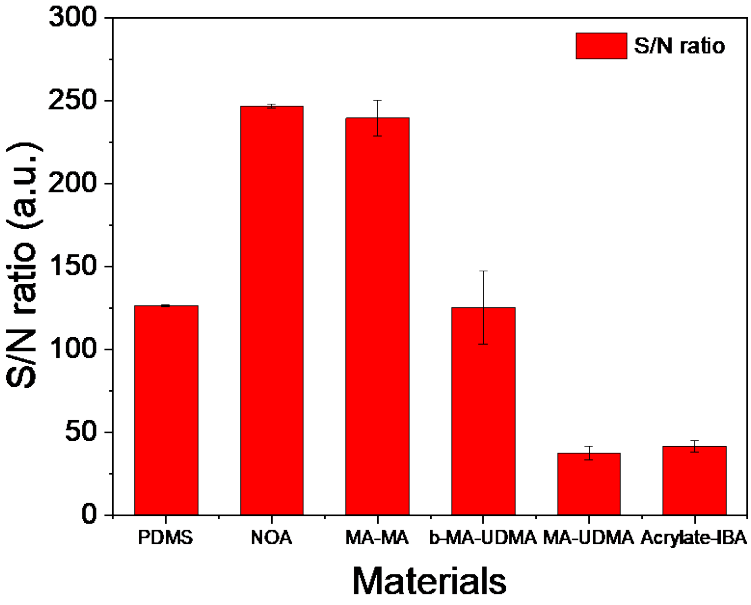

Supplementary figure 11. Fluorescence background intensity test results for different materials for sweat microcuvettes.

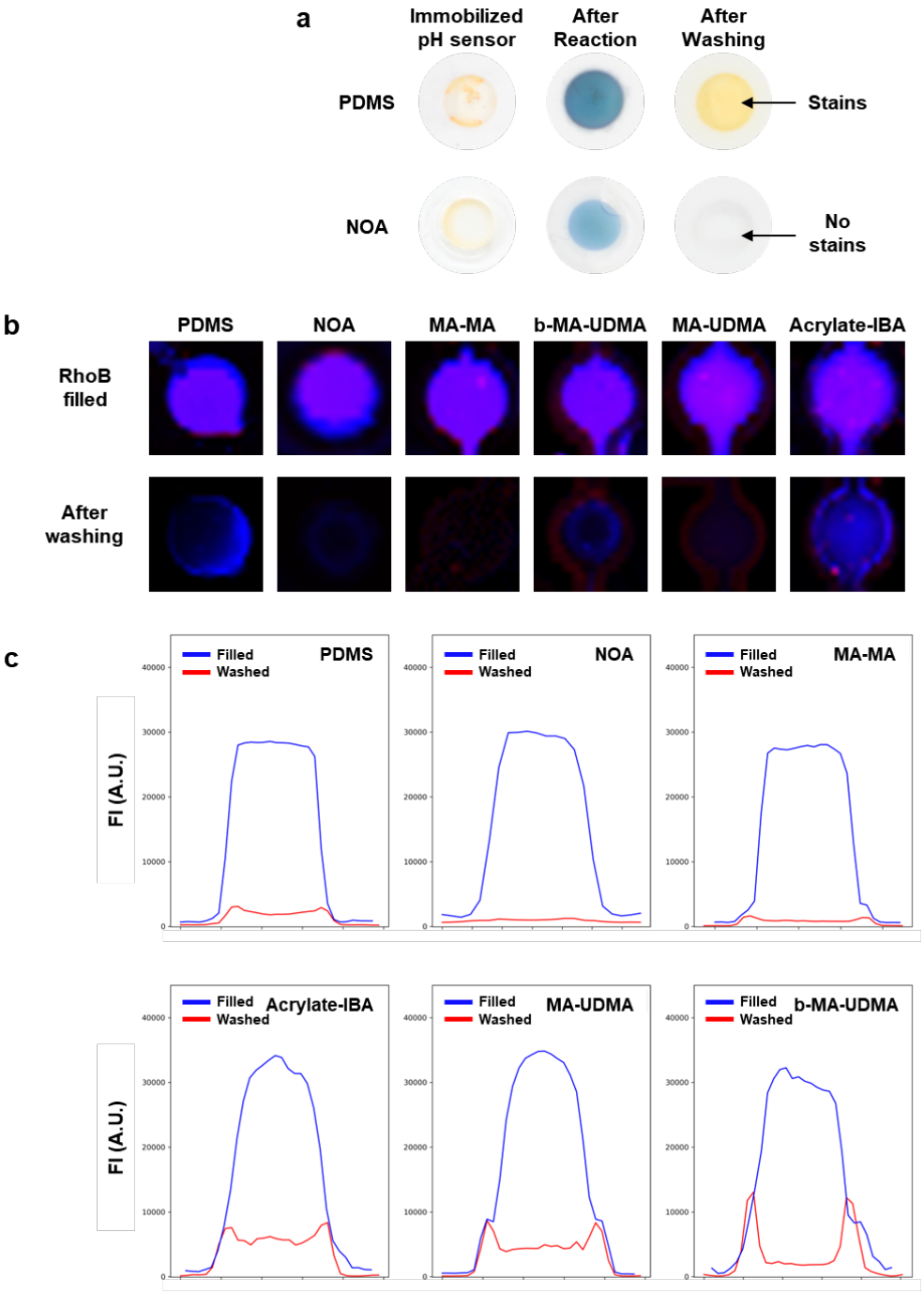

Supplementary figure 12. Absorption test of sweat micro-cuvettes with different cuvette materials. a. Microscopic images of PDMS and NOA sweat micro-cuvette before and after pH sensing. b,c. Absorption of rhodamine B molecules into sweat micro-cuvettes with different materials (PDMS, NOA, MA-MA, b-MA-UDMA, MA-UDMA, Acrylate IBA). Fluorescence images (b) and the associated fluorescent intensity profiles (c) before and after rhodamine B incubation.

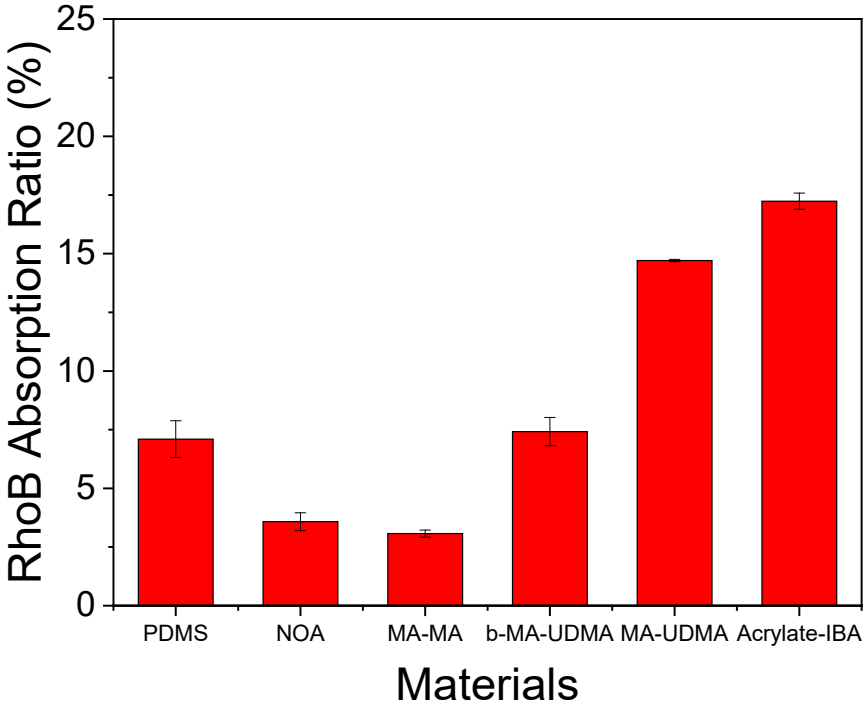

Supplementary figure 13. Fluorescence absorption test results of different materials for sweat microcuvettes.

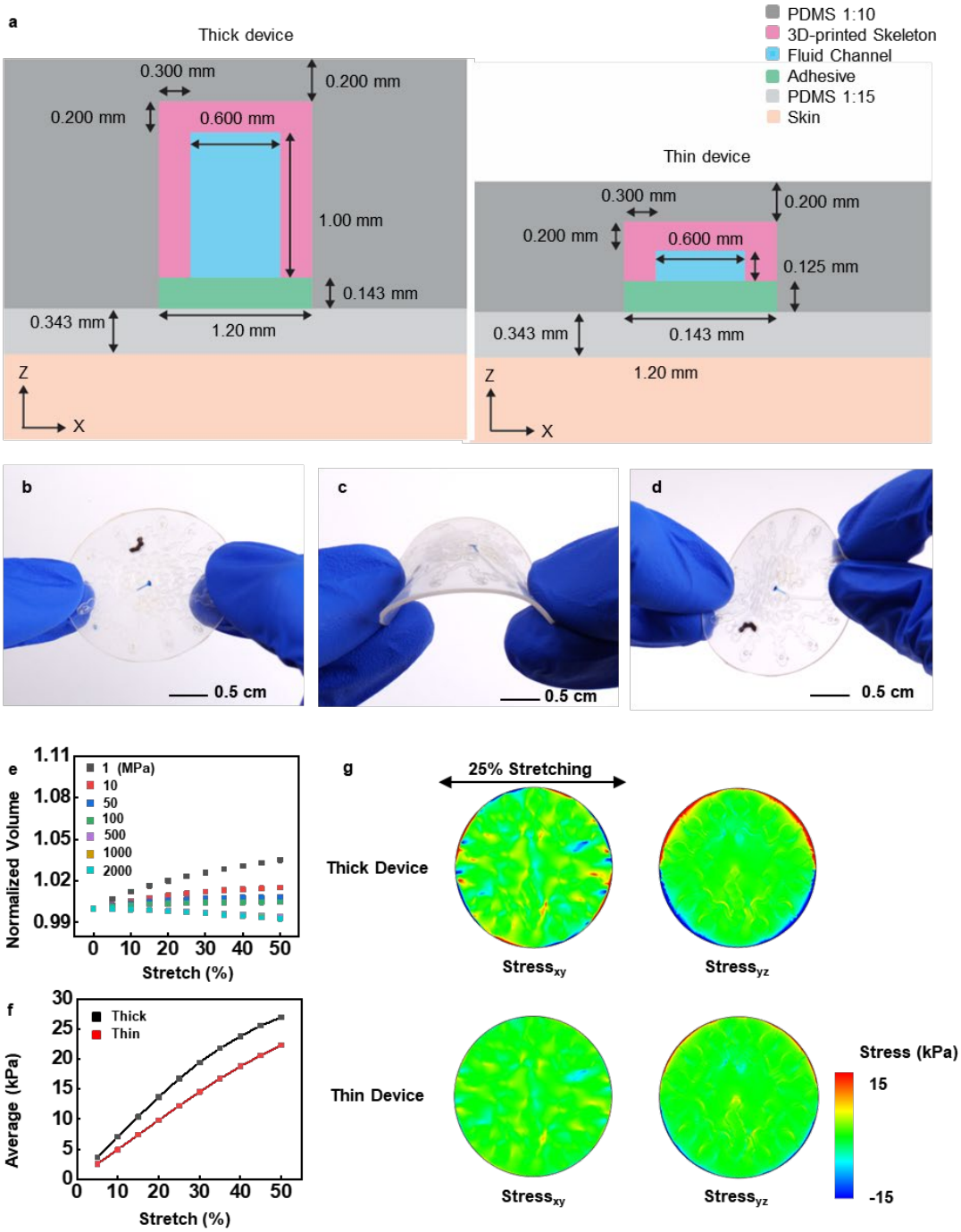

Supplementary figure 14. Mechanical simulations**. a.** Details and key dimensions of the sweat microcuvette structures used in FEA. **b-d.** Photographs of thin sweat microcuvette systems (200 μm) under stretching (30%), bending (radius: 30 mm), and twisting (90°). **e**. Volume change of the thin microcuvette made of materials with various Young's modulus with increasing levels of uniaxial stretch. **f.** Average interfacial stresses on the skin around the 3D-printed sweat microcuvette. **g.** FEA results of contours of interfacial stresses on the skin around the 3D-printed sweat microcuvette device under uniaxial stretching to 25%.

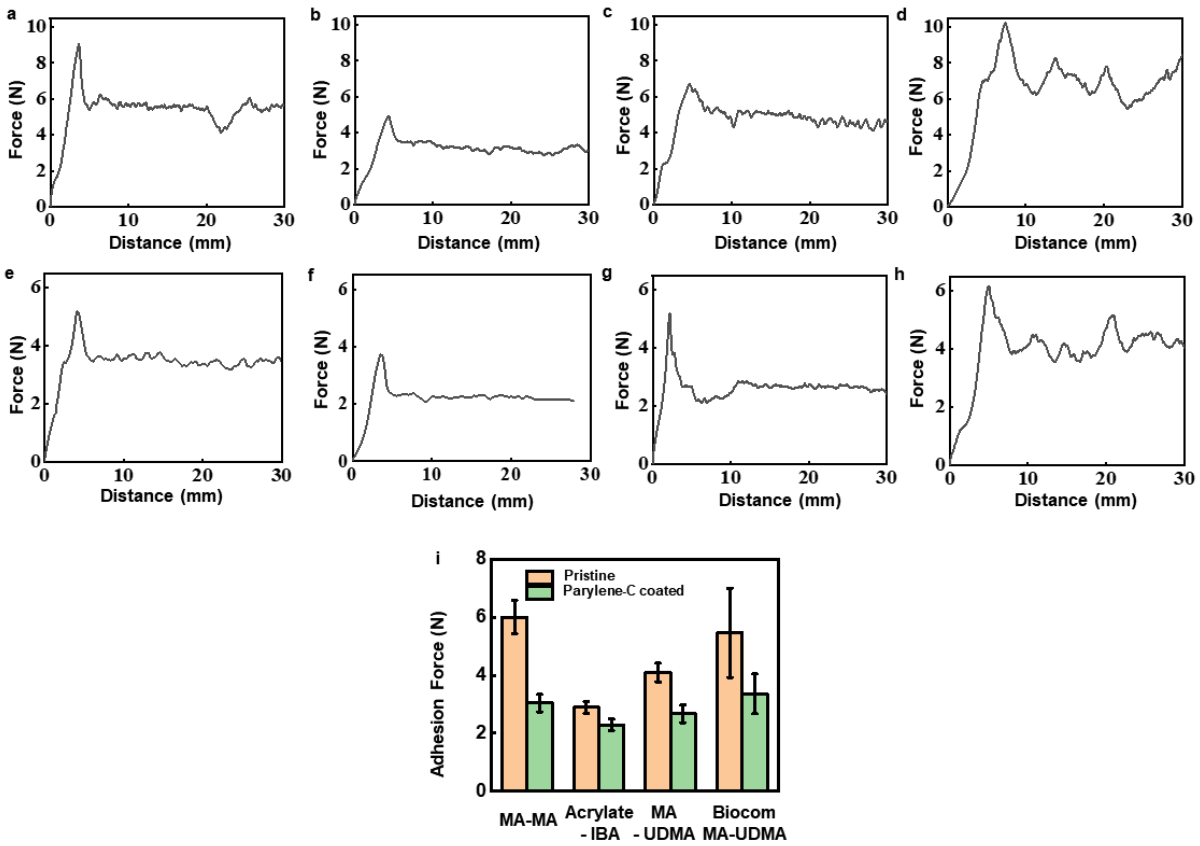

Supplementary figure 15. Adhesion force of the capping layer on microcuvette structures made of various resins. a-h. Force as a function of distance in 180° peel test of capping layers on pristine MA-MA (a), Acrylate-IBA (b), MA-UDMA (c), b-MA-UDMA (d), and Parylene-C coated MA-MA (e), Acrylate-IBA (f), MA-UDMA (g), b-MA-UDMA (h). i. Bar graph summary of the average adhesion force of PDMS on pristine and Parylene-C coated MA-MA, Acrylate-IBA, MA-UDMA, b-MA-UDMA.

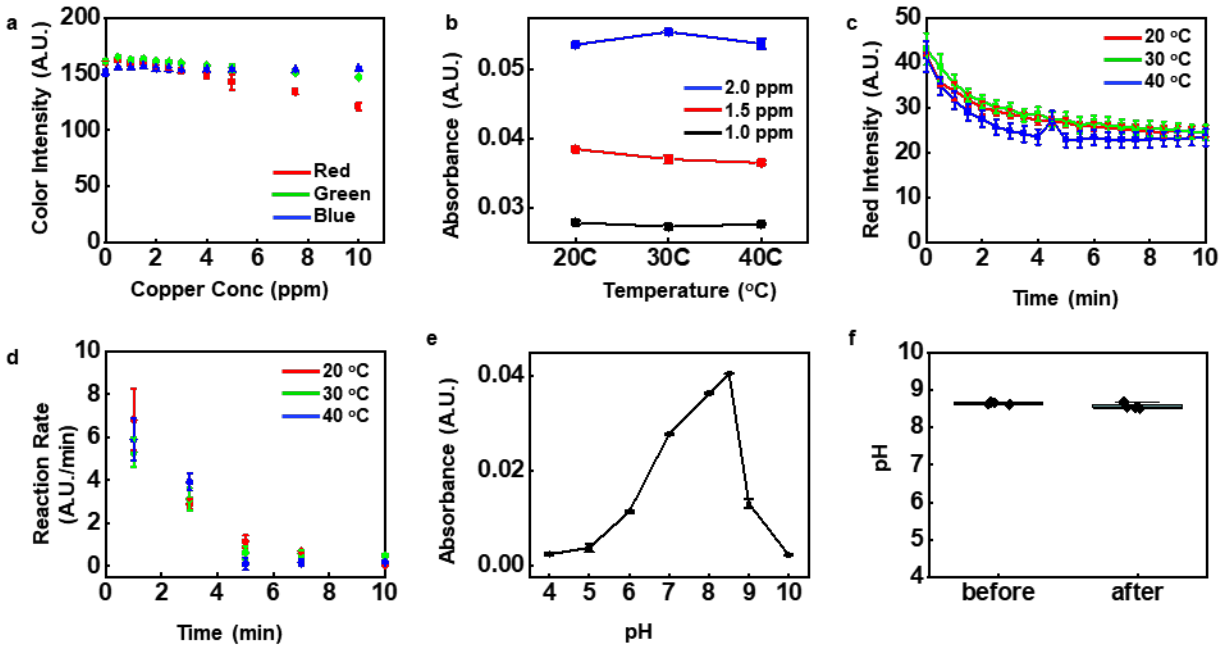

Supplementary figure 16. Characteristics of copper sensor. a. Color level as a function of copper concentration. b. Absorbance according to temperature. c,d. Time dynamics of Cu sensor with different reaction temperature. Red intensity profile(c) and reaction rate(d) according to reaction time with different reaction temperature (20, 30, 40 ℃) e. Absorbance according to pH for assay reacting with 1.5 ppm copper solution. f. pH change after mixing with artificial sweat (pH 4.5).

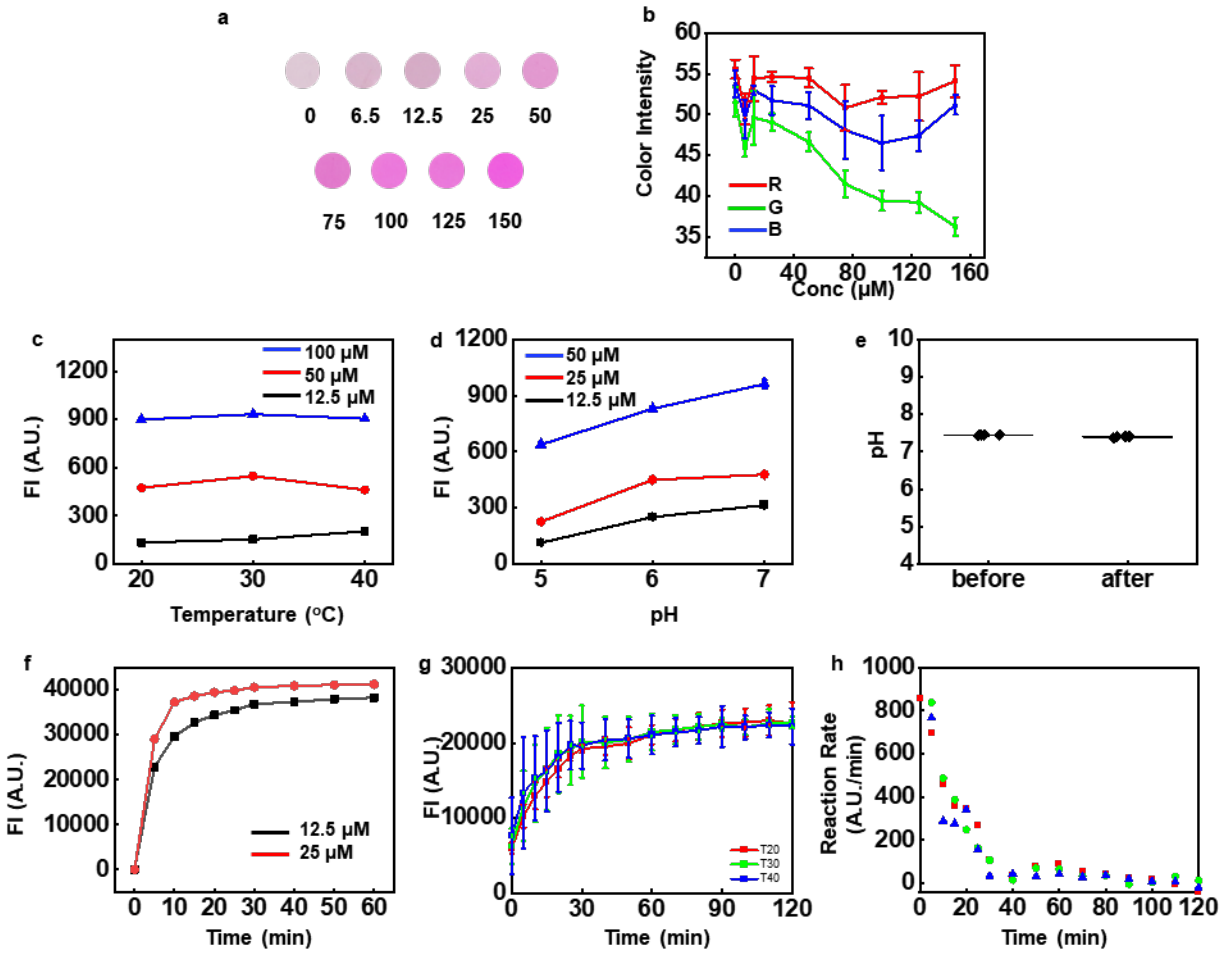

Supplementary figure 17. Characteristics of colorimetric (a-b) and fluorometric (c-h) glucose sensor assays. a. Photograph of color development as a function of glucose concentration. b. Red, green and blue color intensities as a function of glucose concentration. c. Fluorescence intensity change as a function of temperature. D. Fluorescence intensity change as a function of pH. e. pH change after mixing with artificial sweat (pH 4.5). f. Fluorescence intensity development as a function of reaction time. g,h. Time dynamics of the glucose sensor at different reaction temperatures. Fluorescence intensity (g) and reaction rate(h) as a function of reaction time at different reaction temperatures (20, 30, 40 ℃)

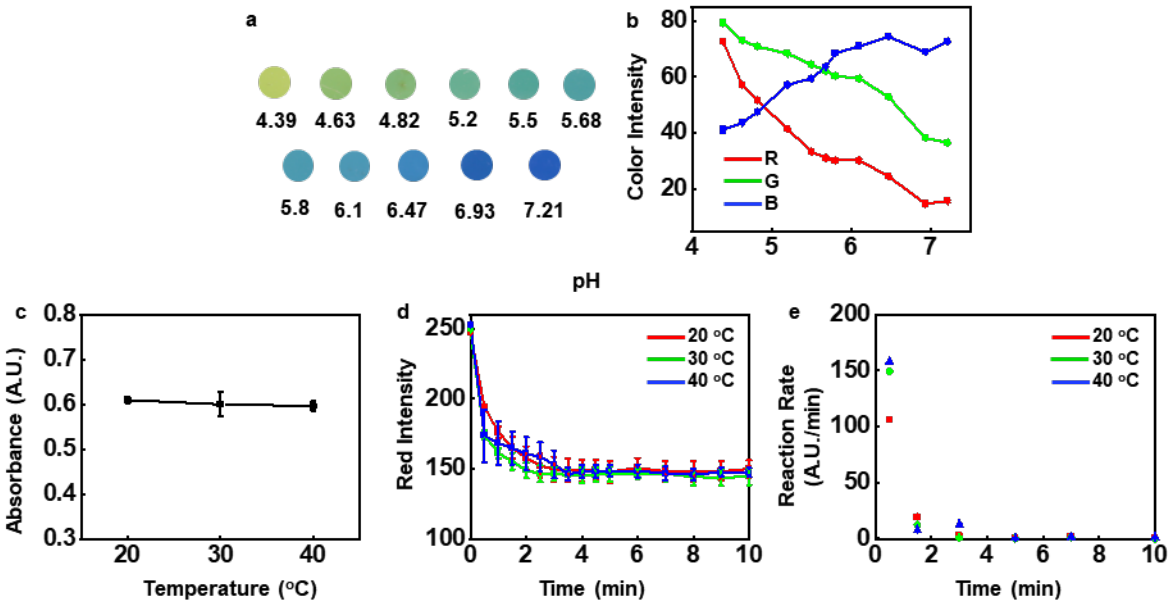

Supplementary figure 18. Characteristics of the colorimetric pH sensor. a. Photograph of color development as a function of pH. b. Red, green and blue color intensities as a function of pH. c. Absorbance change as a function of reaction temperature for pH 7. d,e. Time dynamics of the pH sensor at different reaction temperatures. Red intensity profile(d) and reaction rate(e) of the pH sensor as a function of reaction time at different reaction temperatures (20, 30, 40 ℃).

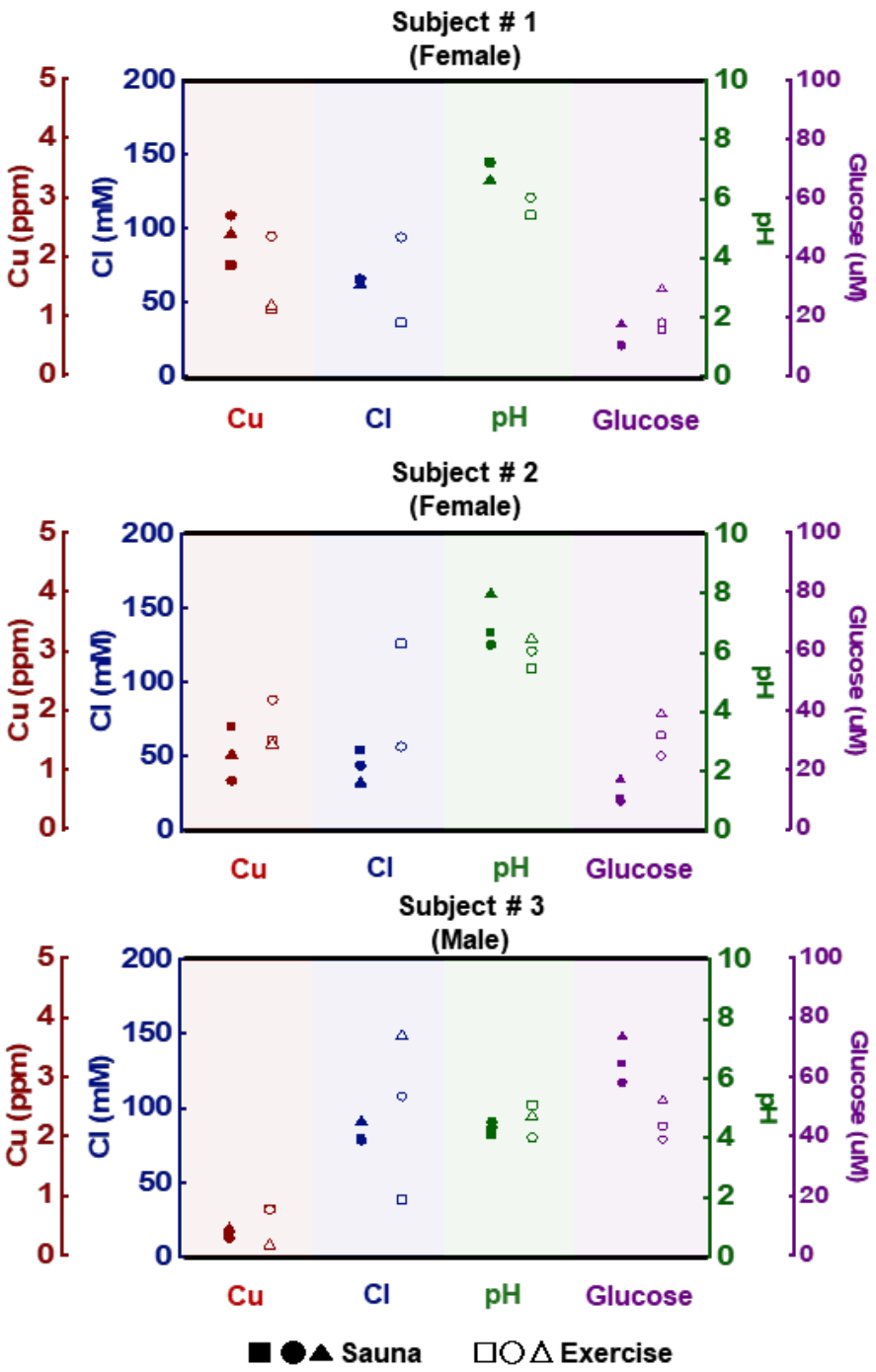

Supplementary figure 19. Comparison between biomarkers (Copper, chloride, pH, glucose) concentrations of sweat collected during sauna or exercise for subject # 1 (a), # 2 (b) and # 3 (c). The different shapes (□, ○, △) indicate different human trials.

Information	MA-MA	b-MA-UDMA	MA-UDMA	Acrylate-IBA
Product Name/ Product Number	Clear /FLGPCL04	Surgical Guide/FLSGAM01	Flexible 80A/ FLFL8001	Elastic 50A/ FLELCL01
Chemical Composition	1. Urethane Dimethacrylate (55-75 wt%) 2. Methacrylic acid, monoester with propane-1,2-diol (15-25 wt%) 3. Diphenyl(2,4,6-trimethylbenzoyl)phosphine oxide (< 0.9 wt%)	1. Urethane Dimethacrylate (55-75 wt%) 2. Methacrylate Monomer (25-45 wt%) 3. Photoinitiator (1-2 wt%)	1. Acrylate Monomer(s) (75-95 wt%) 2. Urethane Dimethacrylate (3-6 wt%)	1. Acrylate Monomer (15-25 wt%) 2. Acrylate Monomer (25-45 wt%) 3. Photoinitiator (<1.5 wt%)
Elongation at Failure (Post-cured)	6.2%	12%	120%	160%
Ultimate Tensile Strength (MPa)	38	> 102	8.9	3.23
Flexural Modulus (GPa)	1.25	> 2.4	N/A	N/A
Tensile Modulus (MPa)	1,600	N/A	6.3 (at 100% Elongation)	1.59 (at 100% Elongation)

Table. S1. Mechanical and chemical information of resins for 3D printing.

Parameters	Effect on sweat sensor accuracy	MA-MA	b-MA-UDMA	MA-UDMA	Acrylate-IBA
Mechanical property	Consistent optical path length	High	High	Low	Low
Transmittance	Molar absorption coefficient	Middle	High	Middle	Middle
Water Barrier	Chemical species concentration in sensing reservoir	High	High	Middle	Middle
Small Molecule Absorption	Chemical species concentration in sensing reservoir	Low	Middle	High	High
Fluorescence Background	Detection limit at low concentration	Low	Middle	High	High

Table. S2. Material properties of resins that affect the sweat sensing accuracy.

Glucose Reaction	Detection limit	Detection Technique	References
Glucose oxidase (GOD)	6.25 uM	Fluorescence	This work
Glucose oxidase (GOD)	30 uM	Color difference in CIELab color space (△E)	[1]
Glucose oxidase (GOD)	10 uM	Color intensity	[2]
Glucose oxidase (GOD)	46 uM	Color intensity, green channel	[3]
Glucose oxidase (GOD)	50 uM	Color intensity, red channel	[4]
Glucose oxidase (GOD)	10 uM	Color intensity, blue channel	[5]
Glucose oxidase (GOD)	50 uM	Color intensity	[6]

Table. S3. Comparison of wearable colorimetric glucose sensors.

pH reaction	Detection limit	Resolution	Detection Technique	References
Customized pH cocktail solution (bromocresol purple, bromocresol green, bromothymol blue)	4.6	0.25	Absorbance	This work
Alizarin red dried in the chamber	3.8	0.5	Color intensity, Green channel,	[3]
Commercial pH test paper	4.0	0.5	Color intensity, Blue channel	[4]
Customized pH cocktail solution (universal pH dye, polyvinyl chloride, o-nitrophenyloctylether, tetrahydrofuran) dried filter paper	4.5	0.5	Color intensity, Red channel	[5]
Universal pH indicator	4.4	0.5	Color intensity	[6]
Customized pH cocktail solution (universal pH dye, polyvinyl chloride, o-nitrophenyloctylether, Aliquat 336, tetrahydrofuran) dried filter paper	4.5	0.5	Color intensity, Red channel	[7]
Customized pH cocktail solution (universal pH dye, polyvinyl chloride, o-nitrophenyloctylether, Aliquat 336, tetrahydrofuran) dried filter paper	5.0	0.5	Color intensity, Red channel	[8]
Customized pH cocktail solution(bromocresol green, bromocresol red violet, and bromothymol blue) dried superhydrophilic nanotextile disk	4.4	0.6	CIE 1931 color space	[9]
Anthocyanin	4.5	0.5	CIE Lab color space, Color differences	[13]

Table. S4. Comparison of wearable colorimetric pH sensors.

Chloride reaction	Detection limit	Detection Technique	References
Silver chloranilate mixture	1 mM	Absorbance	This work
Silver chloranilate mixture	10 mM	CIE Lab color space, Lightness	[5]
Silver chloranilate mixture	10 mM	CIE Lab color space, Lightness	[7]
Customized mixture of 2,4,6-tripyridin-2-yl-1,3,5-triazine (TPTZ), HgSO4 and FeSO4 indicator solution	25 mM	CIE 1931 color space	[9]
Anion exchange paper combined pH test paper	10 mM	CMYK color space, Cyan intensity	[10]
Customized mixture of mercury-(II), ferrous-(II), and 2,4,6-tris(2-pyridyl)-s-triazine (TPTZ)	25 mM	Color intensity, Blue channel	[11]
Silver chloranilate mixture	10 mM	CIE Lab color space, Chroma values with optical filter(green)	[12]
Silver chloranilate mixture	25 mM	CIE Lab color space, Color differences	[13]

Table. S5. Comparison of wearable colorimetric chloride sensors.

Parameters	MA-MA	b-MA-UDMA	MA-UDMA	Acrylate-IBA
Layer thickness	25 μm	50 μm	50 μm	100 μm
Minimum wall thickness	100 μm	200 μm	150 μm	150 μm
Minimum channel width	200 μm	200 μm	300 μm	300 μm

Table. S6. Information of micro-channel designs for 3d printing sweat cuvettes.

[References]

1. Xiao, Jingyu, *et al*. Microfluidic chip-based wearable colorimetric sensor for simple and facile detection of sweat glucose. *Analytical chemistry* **2019**, 9, 23, 14803-14807.
2. Vaquer, Andreu, Enrique Barón, and Roberto de la Rica. Detection of low glucose levels in sweat with colorimetric wearable biosensors. *Analyst* **2021**, 146, 10, 3273-3279.
3. Yue, Xiaoping, *et al*. Simple, skin-attachable, and multifunctional colorimetric sweat sensor. *ACS sensors* **2022,** 7,8, 2198-2208.
4. Liu, Dong, *et al*. Wearable Microfluidic Sweat Chip for Detection of Sweat Glucose and pH in Long-Distance Running Exercise. *Biosensors* **2023,** 13, 2, 157.
5. Choi, Jungil, *et al*. Soft, skin-integrated multifunctional microfluidic systems for accurate colorimetric analysis of sweat biomarkers and temperature. *ACS sensors* **2019**, 4, 2, 379-388.
6. Zhang, Zhong, *et al.* A versatile, cost-effective, and flexible wearable biosensor for in situ and ex situ sweat analysis, and personalized nutrition assessment. *Lab on a Chip* **2019**, 19, 20 3448-3460.
7. Bandodkar, Amay J., *et al*. Battery-free, skin-interfaced microfluidic/electronic systems for simultaneous electrochemical, colorimetric, and volumetric analysis of sweat. *Science advances* **2019**, 5, 1, eaav3294.
8. Zhang, Yi, *et al*. Passive sweat collection and colorimetric analysis of biomarkers relevant to kidney disorders using a soft microfluidic system. *Lab on a Chip* **2019**, 19, 9, 1545-1555.
9. Zhang, Kuikui, *et al*. “Stretchable and superwettable colorimetric sensing patch for epidermal collection and analysis of sweat.” *ACS sensors* **2021**, 6, 6, 2261-2269.
10. Mu, Xuan, *et al*. “A paper-based skin patch for the diagnostic screening of cystic fibrosis.” *Chemical communications* **2015**, 51, 29, 6365-6368.
11. Kim, Sung Bong, *et al.* "Super-absorbent polymer valves and colorimetric chemistries for time-sequenced discrete sampling and chloride analysis of sweat via skin-mounted soft microfluidics." *Small* **2018,** 14,12, 1703334.
12. Ray, Tyler R., *et al*. "Soft, skin-interfaced sweat stickers for cystic fibrosis diagnosis and management." *Science translational medicine* **2021**, 13, 587, eabd8109.
13. Liu, Shanliangzi, *et al*. "Soft, environmentally degradable microfluidic devices for measurement of sweat rate and total sweat loss and for colorimetric analysis of sweat biomarkers." *EcoMat* **2023**, 5, 1, e12270.

Supplementary note 1. Free volume consideration and its effect on the mechanical/chemical properties of resins

The free volume theory of polymers developed by Fox and Flory et. al. [1, 2]. Free volume of polymers can be defined as the volume of free spaces, which is not occupied by polymer chains. As free volume allows diffusion of small molecules including the water, ions, and gases into the polymer film, the water-vapor transmission rate (WVTR) greatly affected by the free volume fraction of polymer(v_f) [3-5].

Water-vapor transmission through polymer film barriers occurs by following steps: 1) water absorption in the polymer, 2) water molecule diffusion, 3) desorption of vapor at the outer side of polymer film barrier. The relationship between free volume of the polymer film and the diffusion coefficient (Dc) was developed by Cohen and Turnbull [3], as shown in **Equation 1**:

$$D_c = g \cdot a^* \cdot u \cdot \exp\left[-\frac{\gamma v^*}{v_f}\right] \qquad \text{Eq. 1}$$

where D_c is the diffusion coefficient, a* is the diameter of the cage, approximately equals the molecular diameter, g is a geometric factor, γ is a numerical factor introduced to correct for overlap of free volume, where between 1/2 and 1, and v_f is the free volume fraction of polymer. v_f is defined by **Equation 2**:

$$v_f = \frac{V_f}{N} \qquad \text{Eq. 2}$$

where V_f is the total free volume and N the number of molecules. v* is of order 10 v_f. So the **Equation 1** could be simplify to the **Equation 3**:

$$D_c = A \cdot \exp\left[-\frac{B}{v_f}\right] \qquad \text{Eq. 3}$$

where A, B are the constants.

Considering the permeability coefficient (P) is the product of the solubility coefficient (S_c) and D_c, Equation 3 could be converted to the following **Equation 4**.

$$P = S_c \cdot D_c = S_c \cdot A \cdot \exp\left[-\frac{B}{v_f}\right] \qquad \text{Eq. 4}$$

Thus, the low free volumes polymer restrains the water or small molecule diffusion in the polymer matrix. As shown in Supplementary table 2, resins with higher water barrier property had lower small molecule absorption property (MA-MA).

As the free volume not only allows the diffusion of small molecules but also allows the local segmental mobility of polymer chain, it affects the mechanical properties as well [4, 6]. From the Williams-Landel-Ferry (WLF) equation, the relation between the young's modulus and free volume fraction of polymer could be described by **Equation 5**, [7]:

$$\log[E(T)] = \log[E(T_r)] + C\left(1 - \frac{v_{f,r}}{v_f}\right) \qquad \text{Eq. 5}$$

Where C is the constant, E(T) is the young's modulus at the temperature T, T_r is the reference temperature, and $v_{f,r}$ is the relative fractional free volume at T_r. As relative free-volume fraction increases, the storage modulus decreases due to the increased configurational entropy [8].

As shown in the Supplementary table 1, rubbery resins with lower modulus (MA-UDMA, Acrylate-IBA) were mainly consisted of acrylate monomer. Substitution of acrylate monomer with methacrylate monomer increase in modulus greatly (MA-MA, b-MA-UDMA). Methyl groups cause steric hindrance for rotary isomerization around bond in the main chain, reducing the kinetic mobility, and subsequently increase in modulus [9].

In summary, free volume of polymer permits diffusion of small molecules and allows the local segmental mobility of polymer chain. The resins with methacylate monomer has lower free volume fraction due to the presence of methyl group, which lead in higher modulus, lower WVTR, and lower small molecule absorption rate **(Supplementary table 1, 2)**. The resin properties based on free volume theory had included in the manuscript for clear explanation.

[Reference]

1. Fox Jr, Thomas G., and Paul J. Flory. Second-order transition temperatures and related properties of polystyrene. I. Influence of molecular weight. *Journal of Applied Physics* **1950**, 21, 6, 581-591.
2. Fujita, Hiroshi. Notes on free volume theories. *Polymer Journal* **1991**, 23, 12, 1499-1506.
3. Cohen, Morrel H., and David Turnbull. Molecular transport in liquids and glasses. *The Journal of Chemical Physics* **1959**, 31, 5, 1164-1169.
4. Hill, A. J., *et al*. Role of free volume in molecular mobility and performance of glassy polymers for corrosion-protective coatings. *Corrosion Engineering, Science and Technology* **2020**, 55, 2, 145-158.
5. Fan, Jiajun, *et al.* Structure dependence of water vapor permeation in polymer nanocomposite membranes investigated by positron annihilation lifetime spectroscopy. *Journal of Membrane Science* **2018,** 549, 581-587.
6. Zhang, H. J., *et al.* Effect of free-volume holes on static mechanical properties of epoxy resins studied by positron annihilation and PVT experiments. *Polymer* **2020**, 190, 122225.
7. Zhang, H. J., et al. Effect of free-volume holes on dynamic mechanical properties of epoxy resins for carbon-fiber-reinforced polymers. *Macromolecules* **2017,** 50, 10, 3933-3942.
8. Matsuoka, S. Free volume, excess entropy and mechanical behavior of polymeric glasses. *Polymer Engineering & Science* **1981**, 21, 14, 907-921.
9. Shevelev, V. A. Study of molecular mobility and interactions in α-methylstyrene-styrene and methylacrylate copolymers using the nmr pulse method. *Polymer Science USSR* **1975**, 17, 2, 460-469.
10. Mikhailov, G. P., and V. A. Shevelev. Study of the motion and steric effects of methyl groups in the α-position in copolymers of methyl methacrylate and methyl acrylate with styrene by means of the NMR impulse method. *Polymer Science USSR* **1968**, 10, 3, 721-731.
11. Lim, Hanpin, and Stephen W. Hoag. Plasticizer effects on physical–mechanical properties of solvent cast Soluplus® films. *Aaps Pharmscitech* **2013**, 14, 903-910.

Supplementary note 2. CFD simulation for evaluation of sweat collection capability of microcuvettes

The flow dynamics and Multiphysics coupling of the air/sweat interface is modeled as a Two-phase flow using the level set interface in COMSOL. The density ρ and dynamic viscosity μ were defined from the values found in the material library for Air and Water, Liquid. In the model, the level set function in air is $\phi = 0$ and in water $\phi = 1$. The transport process can be described by **Equation 1**:

$$\frac{\partial \phi}{\partial t} + \mathbf{u} \cdot \nabla \phi = \gamma \nabla \cdot \left(\varepsilon \nabla \phi - \phi(1-\phi) \frac{\nabla \phi}{|\nabla \phi|} \right) \qquad \text{Eq. 1}$$

Where $\mathbf{u}$ is the fluid velocity, $\varepsilon = \frac{h_c}{2}$ determines the thickness of the interface, h_c is the mesh size of the region and $\gamma = 1$ is a reinitialization parameter. Then the capillary filling is described by the Navier-Stokes equations for transport of mass and momentum for a fluid of constant density as **Equation 2**:

$$\rho \frac{\partial \mathbf{u}}{\partial t} + \rho(\mathbf{u} \cdot \nabla)\mathbf{u} = \nabla \cdot \left[-p\mathbf{I} + \mu\left(\nabla \mathbf{u} + (\nabla \mathbf{u})^{\boldsymbol{T}}\right) \right] + \mathbf{F}_{st} \qquad \text{Eq. 2}$$

Where ρ is the density, μ is the dynamic viscosity, p denotes the pressure. $\mathbf{F}_{st} = \sigma\delta\boldsymbol{\kappa}\mathbf{n}$ is the surface tension force acting at the air/sweat interface where σ is the surface tension coefficient, δ is the Dirac delta function, $\boldsymbol{\kappa}$ is the curvature, and $\mathbf{n}$ is the vector normal to the interface. A 4 μL/min laminar inflow boundary condition was assigned at the inlets and a 0 Pa pressure boundary condition was assigned at the outlets. On the walls there is a no slip boundary condition and a contact angle of 75° is assigned between the wall and the fluid interface. The fluid domains were partitioned to create a mapped mesh with a maximum element size of 0.02 mm. A mesh convergence study was performed to ensure accuracy. The total number of elements in the model is ~50,000.